IOP PUBLISHING PHYSICS IN MEDICINE AND BIOLOGY

Phys. Med. Biol. **52** (2007) 5187–5204 doi:10.1088/0031-9155/52/17/006

List-mode-based reconstruction for respiratory motion correction in PET using non-rigid body transformations

F Lamare[1,2], M J Ledesma Carbayo[3], T Cresson[1], G Kontaxakis[3], A Santos[3], C Cheze Le Rest[1], A J Reader[4] and D Visvikis[1]

[1] INSERM, U650, Laboratoire du Traitement de l'Information Médicale (LaTIM), Brest, F-29200 France
[2] MRC Clinical Sciences Centre, Imperial College, Faculty of Medicine, Hammersmith Hospital, London, UK
[3] ETSI Telecomunicacion Universidad Politecnica de Madrid, Ciudad Universitaria s/n 28040, Madrid, Spain
[4] School of Chemical Engineering & Analytical Science, The University of Manchester, Manchester, UK

Received 14 March 2007, in final form 2 July 2007
Published 9 August 2007
Online at stacks.iop.org/PMB/52/5187

Abstract

Respiratory motion in emission tomography leads to reduced image quality. Developed correction methodology has been concentrating on the use of respiratory synchronized acquisitions leading to gated frames. Such frames, however, are of low signal-to-noise ratio as a result of containing reduced statistics. In this work, we describe the implementation of an elastic transformation within a list-mode-based reconstruction for the correction of respiratory motion over the thorax, allowing the use of all data available throughout a respiratory motion average acquisition. The developed algorithm was evaluated using datasets of the NCAT phantom generated at different points throughout the respiratory cycle. List-mode-data-based PET-simulated frames were subsequently produced by combining the NCAT datasets with Monte Carlo simulation. A non-rigid registration algorithm based on B-spline basis functions was employed to derive transformation parameters accounting for the respiratory motion using the NCAT dynamic CT images. The displacement matrices derived were subsequently applied during the image reconstruction of the original emission list mode data. Two different implementations for the incorporation of the elastic transformations within the one-pass list mode EM (OPL-EM) algorithm were developed and evaluated. The corrected images were compared with those produced using an affine transformation of list mode data prior to reconstruction, as well as with uncorrected respiratory motion average images. Results demonstrate that although both correction techniques considered lead to significant improvements in accounting for respiratory motion artefacts in the lung fields, the elastic-transformation-based correction

leads to a more uniform improvement across the lungs for different lesion sizes and locations.

1. Introduction

One of the parameters affecting quantitation in emission tomography (ET) imaging of the thoracic and abdominal regions is respiratory motion. Respiratory motion has been shown to reduce the accuracy of determining functional lesion volumes and associated recovered activity concentrations (Nehmeh *et al* 2002, Boucher *et al* 2004) influencing positron emission tomography (PET) applications such as radiotherapy treatment planning and response to therapy monitoring, respectively. Furthermore, the introduction of scanning devices combining anatomical and functional imaging has revealed various artefacts in the functional images caused by the use of the anatomical datasets for attenuation correction in combination with associated differences in the respiratory motion conditions during the acquisition of the CT and ET datasets (Goerres *et al* 2002, Visvikis *et al* 2004, Erdi *et al* 2004).

In order to account for respiratory motion effects the gated acquisition of both CT and PET datasets has been suggested as a potential solution. Pan *et al* have demonstrated that the acquisition of a 4D CT can be equally used to derive a truly respiratory average CT that can be subsequently used to correct a PET respiratory average dataset for attenuation effects in the thoracic region (Pan *et al* 2005). On the other hand, using the 4D CT frames to correct a respiratory average PET dataset has been shown to lead to an activity concentration variation of over 30% depending on the phase of the CT frame used for the attenuation correction of the PET images (Erdi *et al* 2004). Similarly, an increase of 36% in the standardized uptake values (SUV) was observed by Nehmeh *et al* when using phase-matched 4D CT frames for the attenuation correction of the corresponding 4D PET frames relative to the use of a static CT scan (Nehmeh *et al* 2004). However, the result of such multi-frame acquisitions leads to gated PET images suffering from poor signal-to-noise ratio since each of the frames contains only part of the counts available throughout the acquisition of a respiration average PET study (Visvikis *et al* 2005). Therefore, the need exists for the development of methodology that corrects for respiratory motion effects between individual gated frames in order to allow the use of the data available throughout a respiratory cycle.

Different authors have attempted to correct the effects of respiratory motion in cardiac ET imaging through the use of either a rigid body transformation of list mode PET datasets (Livieratos *et al* 2005) or through tracking the centre of mass in single photon emission tomography (SPECT) projections (Bruyant *et al* 2003). Although such relatively simple respiratory motion models could be sufficient focusing on single organs such as the heart, it may be inadequate in oncology cases where the thoracic and diaphragmatic areas are of interest. In an attempt to make use of all data available throughout a respiratory gated acquisition for such applications, numerous authors have previously suggested the use of 4D CT datasets to derive transformation maps that could be subsequently used to shift the detected lines of response in the corresponding PET gated frames (Lamare *et al* 2005, 2007, Qiao *et al* 2006, Li *et al* 2006). This work, based on the use of an affine transformation of list-mode data prior to reconstruction, has demonstrated that although this approach leads to significant improvements in lesion contrast and position in the lung fields, it is impossible to use such a model to account at the same time for respiratory motion effects in both the lung fields and organs under the diaphragm. On the other hand, several authors have in the past explored

the use of elastic deformation algorithms to realign individual gated frames suggesting that the resulting deformed gated images could be subsequently summed together making use of all the available data (Klein and Huesman 1997, Dawood *et al* 2006, Visvikis *et al* 2006). However, the summing together of individual gated frames following their reconstruction will obviously lead to inferior quality images than the incorporation of such deformations into the reconstruction process, particularly in the case of using iterative reconstruction algorithms which have become a standard in current clinical practice (Visvikis *et al* 2001, Schoder *et al* 2004, Asma *et al* 2006).

The use of list mode data acquisitions for gated PET may facilitate the *a posteriori* binning of the acquired data. This in turn allows fine temporal sampling and the potential of implementing different binning methodologies reducing the effect of generally observed irregular respiratory motion patterns (Bruyant *et al* 2006). Although the application of a rigid or affine transformation in the raw data domain is feasible considering individual lines of response (Livieratos *et al* 2005, Lamare *et al* 2007), a similar approach for elastic transformation poses obvious challenges. In the past, different approaches for the incorporation of transformations in the system matrix during the reconstruction process have been described (Qi and Huesman 2002, Jacobson and Fessler 2003, Rahmim *et al* 2004, Lamare *et al* 2005, Qiao *et al* 2006, Li *et al* 2006). While the work of Qi and Huesman as well as Rahmim *et al* considered only rigid body transformations, Jacobson and Fessler described the theoretical framework of incorporating non-rigid transformations in the reconstruction algorithm without evaluating the proposed methodology. In addition, Qiao *et al* and Li *et al* evaluated their proposed algorithm on a phantom study simulating only rigid body motion, therefore not allowing the evaluation of elastic transformations in the performance of their algorithm implementation. Finally, the patient study included in Li *et al* was at the level of the pancreas with limited respiratory motion extend of approximately 1 cm and of limited non-rigid nature. The objectives of this study are multiple. Firstly, two different implementations of a list-mode-based reconstruction algorithm incorporating elastic deformations in the system matrix are described and compared using an anthropomorphic phantom, which includes the non-rigid effects of physiological motion at the level of the lung and the diaphragm. Lesions at different locations throughout the lung and liver were included to assess the impact of this correction approach for oncology applications. Secondly, the performance for respiratory motion correction of incorporating elastic transformations in the reconstruction process is compared to the use of an affine transformation applied prior to the reconstruction process (Lamare *et al* 2007). Finally, we establish the qualitative and quantitative image improvements associated with applying the deformation during the reconstruction process of the raw data rather than applying them in individual gated frames which are subsequently summed.

2. Materials and methods

2.1. Simulation study

A digital NURBS-based 4D cardiac-torso phantom (NCAT) was used in the simulation of PET respiratory gated acquisitions (Segars *et al* 2001). A number of different size lesions (7, 11, 15 and 21 mm) were included at different locations throughout the lungs. Normal FDG activity levels were placed in the lung and liver fields, while a tumour to background ratio of 8 to 1 was used. Eight NCAT emission images were produced, corresponding to 0.625 s considering a normal respiratory cycle of 5 s. The first frame represented full exhalation, while the maximum magnitude of respiratory motion (full inspiration) is occurring between the 4th and 5th frames. The model of a clinical PET system (Lamare *et al* 2006) developed

with GATE (Geant4 Application for Tomographic Emission) was combined with the generated NCAT phantom frames in order to obtain dynamic emission images throughout the respiratory cycle. The attenuation images of the NCAT phantom were also integrated in order to simulate the effects of attenuation. Finally, the data simulated for each individual frame was saved in a list mode format.

2.2. Transformation fields

In the clinical case, 3D spatial transformations to be used for the correction of respiratory motion may be obtained through the use of dynamic (respiratory gated) PET/CT datasets, as a number of different authors have already demonstrated (Nehmeh *et al* 2004, Klein and Huesman 1997, Dawood *et al* 2006, Visvikis *et al* 2006). In the simulation study presented here, the generated NCAT attenuation/CT images without any blurring effects (resolution, image statistics effects, etc) were used in combination with an elastic or affine registration algorithm to define the transformation fields to be used during the reconstruction of the simulated list mode emission datasets. Deformation matrices were derived between all individual frames (frames 2–8) and that corresponding to full exhalation (i.e. frame 1, see section 2.1), referred to from here onwards as the reference frame. In the case of the affine registration a normalized mutual information algorithm was employed (Studholme *et al* 1999, Lamare *et al* 2007). On the other hand, respiratory motion compensation fields were also obtained performing independent non-rigid registration processes (Ledesma-Carbayo *et al* 2006) of the NCAT CT frames. The transformation $\mathbf{g}_t(\mathbf{x})$ between frames 2–8 $f(\mathbf{x}, t)$ and the reference $f(\mathbf{x}, 0)$ frame was defined as a linear combination of B-spline basis functions, located in a rectangular grid (Kybic and Unser 2003, Ledesma-Carbayo *et al* 2006, Sorzano *et al* 2005):

$$D_t \equiv \mathbf{g}_t(\mathbf{x}) = \mathbf{x} + \sum_{\mathbf{j}\in\mathbb{Z}^N} \mathbf{c}_\mathbf{j} \beta_r \left(\mathbf{x}/h - \mathbf{j}\right) \tag{1}$$

where $\beta_r(\mathbf{x})$ is a tensor product of centred B-splines of degree r and $\mathbf{j}$ are the indices of the grid locations. The spacing between grid points h determines the number of parameters $\mathbf{c}_\mathbf{j}$ to be optimized and the final rigidity of the solution. The registration is then formulated as an optimization procedure that minimizes the sum of squared differences metric to find the best transformation parameters $\mathbf{c}_\mathbf{j}$. The optimization used a variation of the Marquart–Levenverg nonlinear least-squares optimization in combination with an efficient estimation of the Hessian matrix (Broyden–Fletcher–Goldfarb–Shanno (BFGS)) (Sorzano *et al* 2005). Spline interpolation provides a continuous function of the discrete images, allowing an excellent framework for finding a subpixel solution and to compute analytically the derivatives needed in the optimization process. Speed and robustness are improved by the use of a multiresolution approach in both the image and the transformation space. The multiresolution methodology used creates a pyramid of subsampled images optimal in the L2-sense taking advantage of the spline representation (Unser *et al* 1993). The problem is solved starting at the coarser level of the pyramid (the most subsampled image) and proceeding to the finest level. For each image level two levels of deformation are optimized also following a coarse to fine strategy.

In order to choose the optimal parameters for the particular application in this paper, we performed a set of initial tests. Three different transformation grid spacings were tested: $h = 8, h = 16$ and $h = 32$ pixels. As a result, cubic B-splines with a grid spacing set to $8 \times 8 \times 8$ pixels (8 pixels $\sim$25 mm) provided the best results and were used to represent the deformation. Cubic B-splines were also used for image interpolation and for providing

a continuous representation. The multi-scale processing scheme was set at four levels with successive levels having half size in each dimension.

2.3. Image reconstruction on list-mode data

The one-pass list mode EM (OPL-EM) algorithm (Reader *et al* 2002) was implemented for the reconstruction of the transformed LORs:

$$n_j^{k+1} = \frac{n_j^k}{s_j} \sum_{i \in T^k} p_{ij} \frac{1}{q_i^k} \qquad \text{for} \quad k = 1, \ldots, K \tag{2}$$

where $q_i^k = \sum_{j=1}^{J} p_{ij} n_j^k$ is the expected count in LOR i, p_{ij} is the purely geometric term and represents the geometric probability of detecting at LOR i an event generated in voxel j, n_j is the intensity of voxel j, J is the total number of voxels, s_j is the voxel j of the sensitivity image including the normalization and attenuation corrections and K is the number of time subsets. k is both the iteration number and the subset used in that iteration. T^k is the set of list mode events in the kth subset. The forward projection step was implemented using the accelerated version of the Siddon ray tracing (Siddon 1986, Han *et al* 1999, Zhao and Reader 2002).

An overall sensitivity image S including the normalization and attenuation corrections for each of the individual simulated frames was produced through a forward projection and backprojection of the corresponding NCAT attenuation images. Each voxel s_j of the sensitivity image S is computed as follows:

$$s_j = \frac{1}{N_{\text{frames}}} \sum_{N_{\text{frames}}} \sum_{i \in I} p_{ij} N_i A_i, \qquad \text{with} \quad A_i = \exp\left(- \sum_{j=1}^{J} p_{ij} \mu_j \right) \tag{3}$$

where N_i is the normalization term of the LOR i, A_i is the attenuation correction factor of the LOR i, I is the total number of detectable LORs, J is the total number of voxels and μ_j is the linear attenuation coefficient at the energy of 511 keV (μ_j is the intensity of the voxel j in the NCAT attenuation image) and N_{frames} is the number of temporal gated frames.

2.4. Implementation of elastic transformations in the system matrix

The elastic motion correction can be integrated in a mathematical representation of the system matrix in the PET reconstruction process. If one notes P the system matrix usually describing the PET system, and whose elements p_{ij} represent the geometric probability of detecting at LOR i an event generated in voxel j, the data acquisition in PET can be represented by the equation

$$m = Pf \tag{4}$$

where m are the measured datasets and f is the radioactive distribution. If t_0 corresponds to the reference frame time, the system matrix can be modified to take into account the deformation of the radioactive distribution from time t to time t_0 giving

$$m_t = P_t f \tag{5}$$

where m_t are the measured datasets at time t and f remains the radioactive distribution had the object not moved (i.e corresponding to the reference frame time). The number of system matrices, P_t, corresponds to the number of available PET/CT synchronized frames.

This elastic-based respiratory motion correction can be integrated in any reconstruction process using a representation of the system matrix as described in equation (4), allowing

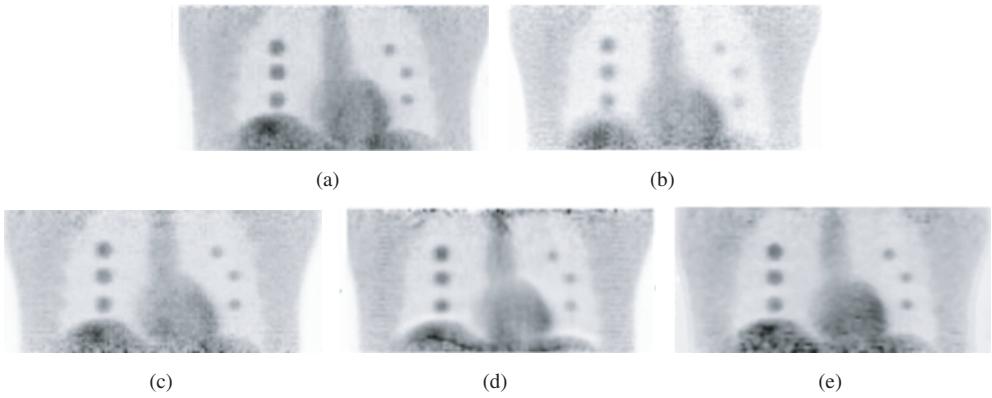

Figure 1. Comparison of the *Frame 1* (a), *Non-Corrected* (b), *LORs-Affine* (c), *Elastic Method 1* (d) and *Elastic Method 2* (e) images. Visual differences can be clearly seen at the levels of the liver and the heart.

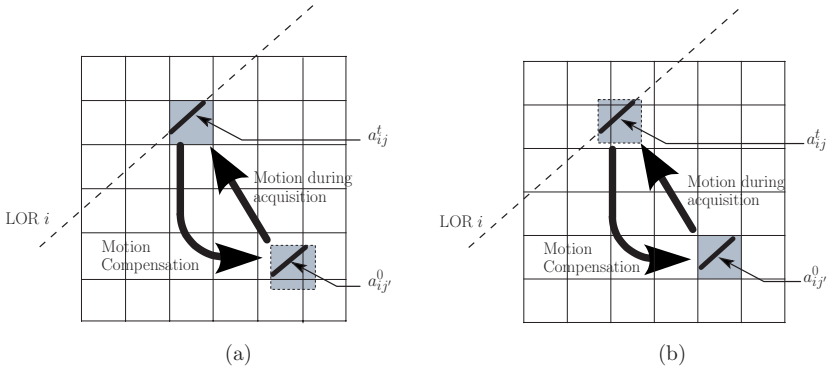

Figure 2. Graphical representation of the incorporation of the elastic motion compensation during reconstruction for (a) the elastic interpolation-based methodology (*Elastic Method 1*) and (b) the elastic direct methodology (*Elastic Method 2*).

the reconstruction of a motion-free image. In our case, the list-mode reconstruction algorithm OPL-EM, given by equation (2), is modified as follows to incorporate the elastic transformations:

$$f^{k+1} = \frac{f^k}{S} \sum_{N_{\text{frames}}} {P_t}^T \frac{1}{P_t f^k} \tag{6}$$

where T is the transpose operator and N_{frames} is the number of temporal gated frames.

In this study, the transformation matrices are provided by the elastic registration described earlier (see section 2.2). The discrete motion deformation matrix D_t contains 3D vectors describing individual voxel motion parameters, such that a voxel j' at time $t_0 = 0$ has been moved to the location $j = D_t(j')$ at acquisition time t (due to object motion). If J is the total number of voxels, the matrix D_t is a $J \times J$ matrix and represents the deformation of the radioactive distribution from time t_0 to time t, on a voxel-by-voxel basis. As figure 2(a) demonstrates the voxel j' at time $t_0 = 0$ (reference image = NCAT frame 1) corresponds to an actual grid voxel, whereas the voxel $j = D_t(j')$ can overlap several voxels of the grid:

$$D_t : \left\{ \begin{matrix} \text{reference} \\ \text{image } (t_0) \end{matrix} \right\} \rightarrow \left\{ \begin{matrix} \text{image at} \\ \text{time } t \end{matrix} \right\} \qquad \text{voxel } j' \rightarrow \text{voxel } j = D_t(j').$$

Assume p_{ij} is the geometric probability of detecting at LOR i an event generated in voxel j. p_{ij} corresponds to the overlap between a voxel j and an LOR i. The overlap between a voxel j and an LOR i at time t is equivalent to the overlap with the transformed voxel j' had the object not moved (reference acquisition time = 0) (see figure 2):

$$p_{ij}^{t}\delta_j \equiv p_{ij'}^{0}, \qquad \text{where} \quad j = D_t(j') \tag{7}$$

where i is the index of the detected LOR, j is the index of the voxel at acquisition time t and j' those of the corresponding motion corrected voxel at time $t_0 = 0$. The function δ_j is defined by

$$\delta_j = \begin{cases} 1, & \text{if the voxel } j \text{ at time } t \text{ is inside the field of view} \\ 0, & \text{otherwise.} \end{cases}$$

The coefficients $p_{ij'}^{0}$ correspond to the coefficients of the system matrix P_t. Since the position of the voxel $j = D_t(j')$ can overlap several voxels of the grid, the accelerated version of the Siddon ray tracing in the implementation of the forward projection step cannot be implemented without an interpolation step. Therefore, in terms of calculating the reconstruction system matrix two different approaches have been evaluated in the current study. The first involves the use of a trilinear interpolation of the coefficient p_{ij}^{t} based on the overlapping volumes of the eight neighbouring voxels (Qiao *et al* 2006) (see figure 2(a)), which subsequently permits the use of the Siddon algorithm for the calculation of the system matrix coefficients. The second approach involves a direct calculation of the coefficients p_{ij}^{t} with the exact location of voxel j at acquisition time t (see equation (7) and figure 2(b)). As the exact location of voxel j at acquisition time t does not match a voxel of the grid, the Siddon algorithm cannot be used to calculate these coefficients (Lamare *et al* 2005). On the one hand, the first approach allows an acceleration of the reconstruction process through the use of the Siddon algorithm while on the other hand it could potentially be introducing errors as a result of the interpolation process in combination with the use of an elastic transformation to derive the displacement matrices D_t. It is worth noting that neither of the two approaches takes explicitly into consideration the deformation of the voxel shape that can be encountered during the use of a non-rigid transformation. However, only the interpolation-based method (through the assumption that the volume of all voxels is the same in the calculation of the overlapping volumes) is affected by such voxel shape deformations.

For both methodologies, the sensitivity image S used to correct for attenuation and normalization has to equally take into account the movement of the voxel location. Therefore, the coefficients s_j of the sensitivity image S are now defined as

$$S = \frac{1}{N_{\text{frames}}} \sum_{N_{\text{frames}}} {P_t}^T N A, \qquad \text{with} \quad A = \exp(-P_t \mu) \tag{8}$$

where μ is the linear attenuation coefficient at the energy of 511 keV in the initial position (μ_j is the intensity of the voxel j in the NCAT attenuation image). N_{frames} is the number of temporal gated frames.

2.5. *Image analysis*

Five different reconstructions were performed:

- The first frame of the respiratory cycle was reconstructed with the same statistics as for the entire respiratory cycle and represents the reference image (*Frame 1* image)
- The eight temporal frames were summed without any transformation and reconstructed (*Non-Corrected* image).

- Each of the list-mode files corresponding to the last seven frames were corrected using the affine registration parameters. They were subsequently summed together and reconstructed using the standard OPL-EM algorithm (*LORs-Affine* image) (Lamare *et al* 2007).
- The elastic transformation fields were included during the reconstruction of the corresponding list-mode datasets (*Elastic Method 1* and *Elastic Method 2* images, corresponding to the implementation of the methodology with and without interpolation, respectively, as described in section 2.4).
- Each of the individual temporal gated frames were reconstructed. The reconstructed images corresponding to the last seven frames were corrected using the elastic parameters cited above and were subsequently summed together (*gated-Frames* image).

Two reconstructed image sizes were considered for the different lesion diameters. Images of $128 \times 128 \times 60$ (voxel size of $3.125 \times 3.125 \times 3.125$ mm^3) and $256 \times 256 \times 120$ (voxel size of $1.5625 \times 1.5625 \times 1.5625$ mm^3) were obtained for each of the reconstructed temporal NCAT frames with the lung lesions of 15, 21 mm and 7, 11 mm in diameter, respectively. For a list mode dataset of 10 million detected coincidences, an iteration of the OPL-EM algorithm was <4 min for an image of the above dimensions (Intel Xeon 3 GHz dual core). A total of seven iterations were found to be optimum for the reconstruction of the NCAT images. Using the interpolation- and the non-interpolation-based approaches in the implementation for the incorporation of the non-rigid transformations in the reconstruction system matrix increased the time of acquisition by less than 5% and over a factor of 10, respectively.

The motion corrected images using the affine model and the two different implementations of the elastic model were compared to the first temporal frame (*Frame 1* = reference image). The total number of coincidences were kept the same for all images in order to distinguish the effects purely associated with motion, rather than including those arising from differences in statistical quality between the single temporal frame (including only part of the data) and the corrected frames (including all of the available data). In order to better quantify motion compensation, we have also compared the motion corrected images with the respiratory average image (*Non-Corrected*).

The percent relative difference (PRD) of the radioactivity concentration (Lamare *et al* 2007) was used to quantify the improvement in terms of contrast, position and FWHM of the simulated lesions. The PRD is computed as

$$\%\mathrm{PRD} = \left| \frac{\mathrm{Evaluated} - \mathrm{Frame\ 1}}{\mathrm{Frame\ 1}} \right| \times 100 \tag{9}$$

where the variable *Evaluated* can be either the *LORs-Affine*, the *gated-Frames*, the *Non-Corrected* or the *Elastic* image. Based on the calculated PRD, the contrast and FWHM improvements as a result of the respiratory correction are computed using

$$\%\mathrm{improvement} = \frac{\mathrm{PRD}_{\mathrm{Corrected}} - \mathrm{PRD}_{\mathrm{Non\text{-}Corrected}}}{\mathrm{PRD}_{\mathrm{Non\text{-}Corrected}}} \times 100 \tag{10}$$

where the variable *Corrected* can be either the *LORs-Affine*, the *gated-Frames* or the *Elastic* image.

To assess the improvement in terms of contrast in the reconstructed images, regions of interest (ROI) were placed in each of the lung lesions and in the background lung. The slice with the maximum count density over the lesion was identified for the ROI analysis. Average count densities were subsequently derived for each lesion.

On the other hand, to quantify the position and FWHM improvement as a result of the motion compensation, line profiles were drawn in the x-, y- and z-directions for each lesion.

Table 1. Contrast improvement analysis (equation (10)) on a lesion by lesion basis in the lung field through comparison of the Non-Corrected and Corrected images. Results are shown for both correction approaches *Elastic Method 1* and *Elastic Method 2*.

% Contrast improvement	Lesion diameter (mm)	Elastic Method 1	Elastic Method 2
Upper lobes of the lungs	15	78.08	94.11
	21	86.41	94.80
Middle lobes of the lungs	15	73.82	88.99
	21	83.90	99.39
Lower lobes of the lungs	15	65.88	95.28
	21	90.38	98.25

Table 2. Position improvement analysis (equation (10)) of the different size lung lesions along the *Y*- and *Z*-axes. Results are shown for both correction approaches *Elastic Method 1* and *Elastic Method 2*.

% Position improvement	Lesion diameter (mm)	Elastic Method 1		Elastic Method 2	
		Y	*Z*	*Y*	*Z*
Upper lobes of the lungs	15	91.15	90.16	96.48	96.48
	21	76.90	79.54	98.64	95.17
Middle lobes of the lungs	15	84.34	78.83	92.65	94.60
	21	84.79	93.65	78.84	96.07
Lower lobes of the lungs	15	91.04	94.88	94.66	97.50
	21	62.55	88.87	86.64	97.41

Table 3. FWHM improvement analysis (equation (10)) of the different size lung lesions along the *Y*- and *Z*-axes. Results are shown for both correction approaches *Elastic Method 1* and *Elastic Method 2*.

% FWHM improvement	Lesion diameter (mm)	Elastic Method 1		Elastic Method 2	
		Y	*Z*	*Y*	*Z*
Upper lobes of the lungs	15	73.37	60.62	93.96	84.55
	21	81.00	75.85	81.89	87.02
Middle lobes of the lungs	15	47.95	90.06	92.39	99.26
	21	77.20	96.81	94.26	97.40
Lower lobes of the lungs	15	73.84	86.58	90.13	92.22
	21	94.45	68.20	92.74	92.65

Each of the lung lesion profiles was subsequently fitted with a Gaussian in order to derive the position and FWHM in all three dimensions.

3. Results

Tables 1–3 allow the direct comparison of the two elastic methodologies presented in terms of contrast, position and FWHM improvements, respectively. For all these three parameters,

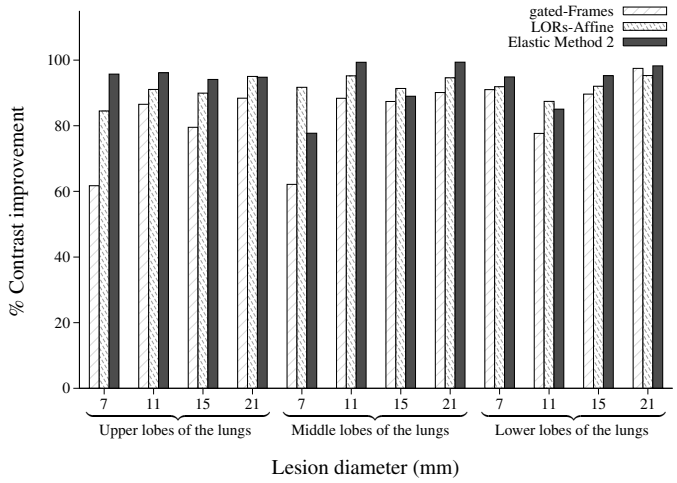

Figure 3. Contrast improvement due to the two respiratory motion correction techniques.

the direct-calculation-based methodology (see section 2.4) demonstrates better results than the trilinear interpolation-based method. The average difference in terms of contrast improvement between the two methods is ∼13%. Concerning the position improvement the difference between the two methodologies is on average ∼11% and ∼9% along the *Y*- and the *Z*-axis, respectively. Finally in terms of FWHM, the improvements observed on the *Elastic Method 2* image are higher by an average of 20% and 11% along the *Y*- and the *Z*-axis, respectively, in comparison to the interpolation-based approach (*Elastic Method 1* image).

The results obtained for the *LORs-Affine* image reconstruction methodology are those presented in (Lamare *et al* 2007) and included here for completeness and in order to facilitate an easy comparison to the performance of the elastic-transformation-based approaches evaluated in this work. The relative difference in terms of contrast between the reference image (i.e. *Frame 1*) and the other reconstructed images (see section 2.5), including the different correction approaches evaluated in this work, is shown in table 4. Using the results from table 4 and equation (10) the contrast improvement results for *gated-Frames*, *LORs-Affine* and *Elastic Method 2* images are shown in figure 3. A significant contrast improvement of the lung lesions (between 85% and 99%) can be seen as a result of the elastic transformation. In addition, the contrast improvement in both *gated-Frames* and *LORs-Affine* images is, for all the lesion sizes, lower than with the *Elastic Method 2* image.

On the other hand, in the case of the affine transformation, the contrast of the liver lesions (independently of their size) was higher by a maximum of 10%, which is significantly less than the minimum improvement obtained for the lung lesions. This was to be expected since as already mentioned in (Lamare *et al* 2007) a common set of transformation parameters (i.e. in this case those of the lung) does not correct for respiratory effects on organs below the diaphragm. With the *Elastic Method 1* and *Elastic Method 2* images, the contrast improvement on the liver lesions was <55% and ∼77%, respectively. The worst performance of the *Elastic Method 1* image is most probably due to the inaccuracies introduced by the trilinear interpolation methodology in the area of the diaphragm suffering from large elastic deformations.

The corrected image should be similar to the first frame of the respiratory cycle. The percentage differences in terms of the lesion spatial position and FWHM relative to the reference image are summarized in tables 5 and 6.

Table 4. Contrast per cent relative difference analysis (equation (9)) on a lesion by lesion basis in the lung field through comparison of the Non-Corrected and Corrected images. Results are shown for both approaches of applying the transformation in the raw data prior to the reconstruction process (*LORs-Affine*) as well as in the images and subsequently summing them together (*gated-Frames*) or integrating the elastic transformation parameters within the reconstruction process (*Elastic Method 1*).

Contrast	Lesion diameter (mm)	Non-Corrected	gated-Frames	LORs-Affine	Elastic Method 2
Upper lobes of the lungs	7	28.30	10.83	4.39	1.21
	11	31.48	4.23	2.82	1.21
	15	30.33	6.20	3.05	1.79
	21	12.96	1.50	0.65	0.67
Middle lobes of the lungs	7	18.87	7.14	1.56	4.20
	11	28.86	3.35	1.38	0.19
	15	30.87	3.89	2.66	3.40
	21	21.16	2.09	1.14	0.13
Lower lobes of the lungs	7	32.42	2.92	2.63	1.66
	11	35.35	7.89	4.45	5.28
	15	38.68	4.01	3.07	1.82
	21	27.56	0.69	1.30	0.48

Table 5. Position per cent relative difference analysis (equation (9)) of the different size lung lesions along the *Y*- and *Z*-axes. Results are shown for both approaches of applying the transformation in the raw data prior to the reconstruction process (*LORs-Affine*) as well as in the images and subsequently summing them together (*gated-Frames*) or integrating the elastic transformation parameters within the reconstruction process (*Elastic Method 1*).

Position	Lesion diameter	Non-Corrected		gated-Frames		LORs-Affine		Elastic Method 2	
Y/*Z*	(mm)	*Y*	*Z*	*Y*	*Z*	*Y*	*Z*	*Y*	*Z*
Upper lobes of the lungs	7	0.76	4.67	0.83	0.79	0.52	1.06	0.36	0.40
	11	0.65	3.37	0.57	0.51	0.37	1.40	0.18	0.28
	15	2.69	7.38	0.08	0.36	0.11	0.43	0.09	0.26
	21	1.51	5.62	0.14	0.33	0.08	0.59	0.02	0.27
Middle lobes of the lungs	7	1.19	3.87	0.38	0.49	0.36	1.81	0.27	0.61
	11	2.16	3.83	0.10	0.61	0.20	0.60	0.06	0.59
	15	0.84	4.27	0.09	0.36	0.13	0.74	0.06	0.23
	21	2.02	5.76	0.68	0.71	0.54	0.34	0.43	0.23
Lower lobes of the lungs	7	3.35	9.34	0.38	0.29	0.27	0.57	0.09	0.17
	11	2.28	2.47	1.43	0.43	1.09	0.43	0.66	0.38
	15	1.71	4.63	0.15	0.24	0.28	0.65	0.09	0.12
	21	2.23	5.18	0.33	0.16	0.34	0.12	0.30	0.13

Figure 4 shows the profile response of the lesions in the respiratory corrected images, compared with the NCAT reference frame image. According to the profile in the *Z*-direction, one can appreciate that the displacement of the lesions is well corrected in the *Elastic Method 2* image in comparison to the NCAT gated *Frame 1* and the uncorrected respiration average image, resulting in a spatial location improvement of between 85% and 99%. It is worth noting the drop in the voxel intensity in the corrected *Elastic Method 1* image at the position of the diaphragm that can be once more attributed to the large elastic deformations in this area

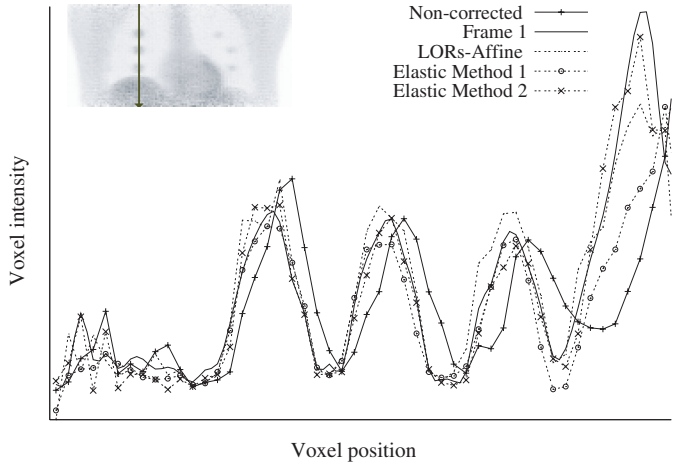

Figure 4. Profile of the lung lesions and the liver along the *Z*-axis.

Table 6. Per cent relative difference analysis (equation (9)) of the FWHM of the different size lung lesions along the *Y*- and *Z*-axes. Results are shown for both approaches of applying the transformation in the raw data prior to the reconstruction process (*LORs-Affine*) as well as in the images and subsequently summing them together (*gated-Frames*) or integrating the elastic transformation parameters within the reconstruction process (*Elastic Method 1*).

FWHM	Lesion diameter	Non-Corrected		gated-Frames		LORs-Affine		Elastic Method 2	
Y/*Z*	(mm)	*Y*	*Z*	*Y*	*Z*	*Y*	*Z*	*Y*	*Z*
Upper lobes	7	4.28	7.14	1.89	0.56	0.89	0.36	0.84	0.28
of the lungs	11	22.89	9.35	2.29	0.65	1.46	2.26	0.64	0.27
	15	4.84	2.46	0.45	1.89	0.50	1.22	0.29	0.38
	21	12.48	7.69	4.31	1.34	3.99	1.47	2.26	1.00
Middle lobes	7	25.32	26.47	2.25	3.22	7.25	3.56	1.78	3.06
of the lungs	11	9.61	5.78	0.64	1.51	0.71	2.17	0.42	0.88
	15	9.60	17.84	3.19	1.77	1.69	1.25	0.73	0.13
	21	5.48	9.28	2.55	0.30	1.55	0.99	0.31	0.24
Lower lobes	7	23.48	48.61	2.49	4.91	2.69	4.81	1.11	5.06
of the lungs	11	10.51	12.77	0.45	0.83	1.02	1.48	0.34	0.61
	15	3.05	15.79	0.80	2.12	1.09	1.64	0.30	1.23
	21	6.72	5.48	0.54	1.74	0.75	1.02	0.49	0.40

in combination with the use of the interpolation in the reconstruction process. The *z* position of the lesions in the *gated-Frames* or *LORs-Affine* images is less well corrected than in the *Elastic Method 2* image. The average improvement difference in the corrected images is over 10% and 20% for the *LORs-Affine* and *gated-Frames* image, respectively. Along the *Y*-axis, the position improvement extends from 65 to 99% for the *Elastic Method 2* image, while the difference with the two other corrected images remains roughly the same.

Figures 5–8 contain the results on the FWHM along the *y*- and *z*-directions for the lung lesions as a function of lesion size and location. The respiratory motion in the NCAT phantom is very small along the *X*-axis, so the improvement results in this direction are not been presented. Concerning the FWHM of the lesion profiles along the *Z*-axis, the maximum improvement is ∼99%. For the three parts of the lung considered, the maximum improvement is obtained

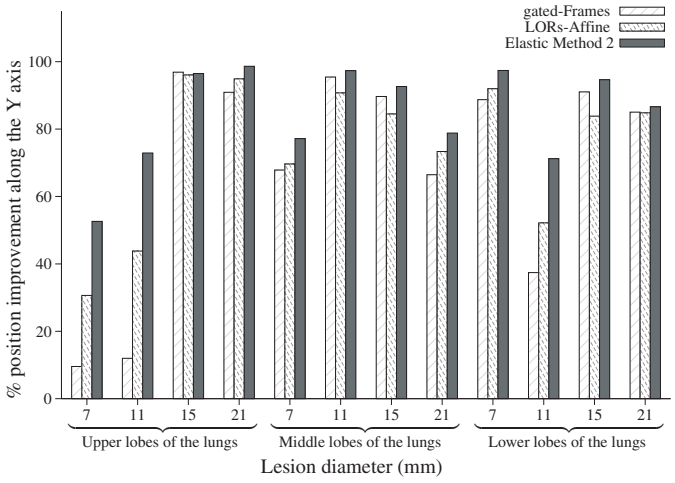

Figure 5. Percentage improvement of the position of the different sizes lung lesions along the *Y*-axis.

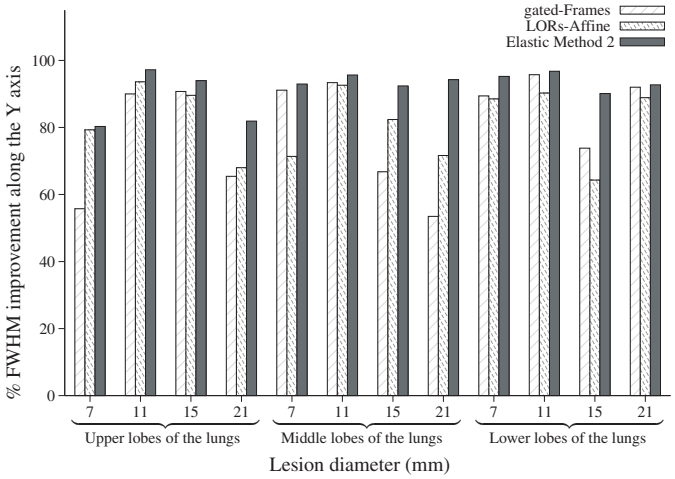

Figure 6. Percentage improvement of the FWHM of the different sizes lung lesions along the *Y*-axis.

for the bigger lesions, considering that we are limited on our improvement estimation by the relative size of the smaller lesions in comparison to our reconstructed pixel size.

Finally, the profiles in figure 9 serve to demonstrate the significant respiratory motion correction obtained using the elastic-transformation-based approach relative to the limited impact from the application of an affine transformation using lung parameters for the organs below the diaphragm, such as the liver.

4. Discussion

The acquisition of gated frames for the correction of respiratory motion in whole body PET/CT imaging results in some motion compensation. On the other hand, however, gated images are suffering from reduced signal-to-noise ratio as they contain only part of the data

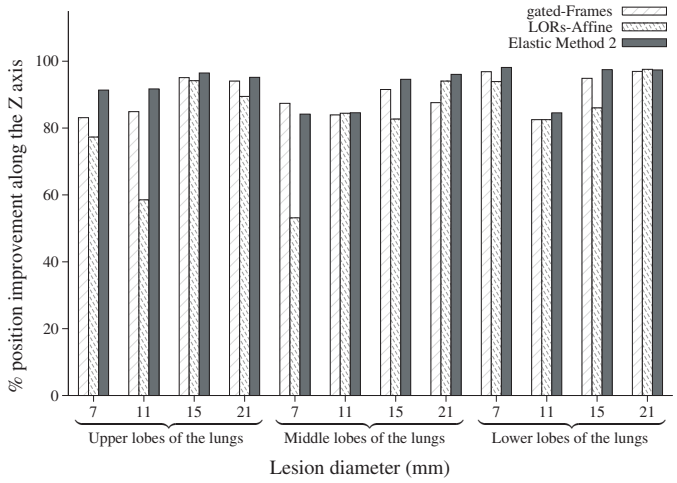

Figure 7. Position improvement along the *Z*-axis due to the two respiratory motion correction techniques.

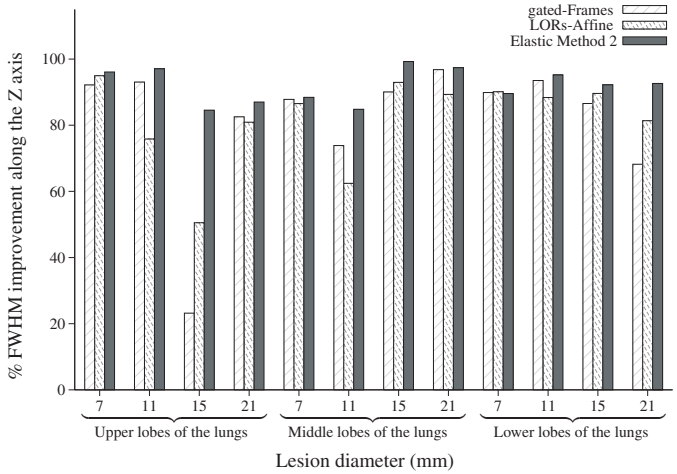

Figure 8. FWHM improvement along the *Z*-axis due to the two respiratory motion correction techniques.

available throughout a respiratory motion average emission acquisition. A simulation study has previously demonstrated that the overall time of a 4D acquisition needs to be increased by at least a factor of 2–3 relative to a static acquisition before realizing any improvements in terms of respiratory motion compensation from gated acquisitions (Visvikis *et al* 2004). As a result, different approaches have been suggested for the correction of respiratory motion differences between gated frames that may eventually allow their combination in a particular position of the respiratory cycle. The vast majority of these approaches are based on the use of image registration techniques for the realignment of individual gated frames. Although subsequent summing of the registered gated frames has been suggested, a correction applied either prior or during the reconstruction process should lead to superior results in terms of contrast and signal-to-noise ratio (Lamare *et al* 2007), particularly considering the use of iterative reconstruction algorithms which have become a standard in clinical whole body

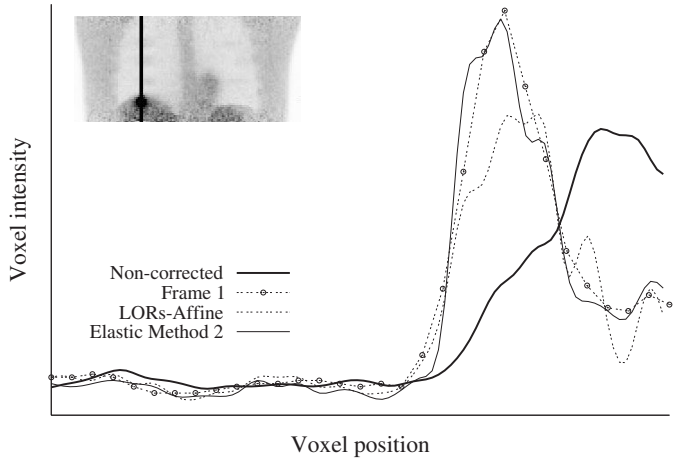

Figure 9. Profiles across the liver lesion (21 mm in diameter) along the *Z*-axis.

imaging. In such an implementation the transformation fields derived between individual gated images are used to either shift the data prior to the reconstruction (rigid- or affine-model-based transformation) or during the reconstruction (non-rigid-based transformation). Such transformations can be derived using either reconstructed 4D PET (Dawood *et al* 2006, Visvikis *et al* 2006) or 4D CT images (Visvikis *et al* 2006, McClelland *et al* 2006). Rigid or affine transformations may account for respiratory motion effects in single organs or lesions (Livieratos *et al* 2005, Lamare *et al* 2007, Bruyant *et al* 2003). However, accounting for respiratory motion effects in the whole field of view may require a non-rigid registration methodology. The purpose of this work has been to describe a couple of different approaches for the incorporation of elastic transformations in the reconstruction of list mode data and compare their performance relative to an affine-model-based transformation taking place prior to the reconstruction process. Furthermore, the qualitative and quantitative accuracy in the corrected images associated with using the non-rigid transformations during the reconstruction process rather than applying it to reconstructed images that can be subsequently summed together was also evaluated.

The NCAT phantom, describing a realistic motion model including non-rigid motion, effects was used in this study. Lesions of variable size and location in the lung and liver fields were introduced. Both affine and elastic transformation parameters were derived by using the non-noisy high-resolution NCAT-phantom-based attenuation maps, in order to minimize errors in the image-based-derived transformation parameters. Two different methodologies for the modification of a list-mode-based image reconstruction algorithm in order to allow the incorporation of elastic transformations during the reconstruction process of 4D acquired datasets have been described. Dedicated attenuation and normalization corrections were also developed to take into account the applied elastic transformations.

The main difference in the two implementations of the reconstruction algorithm presented in this paper is based on the fashion of incorporating the transformation parameters in the reconstruction system matrix. In the first approach, a trilinear interpolation is employed (Qiao *et al* 2006) during the calculation of the sensitivity image coefficients following their displacement in the reconstruction matrix based on the transformation fields for each of the gated datasets. The second approach involves a direct calculation of these coefficients based on their new position without the need for an interpolation step. Although the introduction of an interpolation step allows the use of the Siddon algorithm, significantly

reducing reconstruction times, it suffers by the assumption governing the interpolation step. This interpolation is based on the overlapping volumes of the eight neighbouring voxels (see section 2.2), the assumption being that the non-rigid transformation operations performed to obtain the necessary displacement vectors do not significantly alter the shape of the voxels. Such an assumption, although valid for small displacements, can be questioned for areas where significant non-rigid body movements take place. In our investigation with the NCAT phantom, the area of the diaphragm presents the largest non-rigid deformations induced by the respiratory motion. As demonstrated in figure 1(e), white band artefacts appear in the area of the diaphragm. The corresponding loss of voxel intensity is also shown in figure 4. In addition, as far as quantitative results are concerned, the interpolation-based methodology performed globally worse than the direct-calculation-based implementation by $<13\%$ as far as lesion contrast and position recovery are concerned and up to 20% in the lesion size improvements. These differences occurred in their large majority considering the lesions closer to the diaphragm. At the same time, the direct-based method renders the reconstruction process slower by over a factor of 10.

A comparison of the reconstructed images with and without transformation applied on the raw list mode datasets revealed significant respiratory motion compensation in the lungs. As figure 3 demonstrates an improvement of $\sim$85–99% in terms of contrast on lung lesions in the corrected images was obtained. In terms of improvements on lesion location and size there was a more non-uniform recovery depending on the placement of the lesion in the lung field varying from 70% to 95% and from 80% to 97%, respectively.

The corrected images based on the use of elastic transformations in the reconstruction process were compared to the results obtained through the use of a previously described affine-based model, where the transformation of list mode data takes place prior to the reconstruction (Lamare *et al* 2007). In terms of contrast improvements of up to 30% in comparison to the affine-transformation-based correction were obtained. A larger improvement was generally observed for the smaller lesions placed in the lower part of the lung fields, leading to an overall more uniform correction throughout the lungs relative to the affine-transformation-based approach, irrespective of the lesion size and location.

Finally, a superior contrast by on average between 20% and 30% was observed in the recovered lesion contrast as a result of performing the correction prior to the reconstruction process rather than using the spatial transformation parameters for adjusting individual gated images and subsequently summing them together. On the other hand, differences obtained between the recovered position and size of the lesions between the image-based and the raw-data-based solution were on average less than 10%.

In summary, the developed methodology has demonstrated that the application of an elastic spatio-temporal transformation during the reconstruction process of gated PET datasets leads to significant improvements in overall image qualitative and quantitative accuracy, making use of all available data throughout a respiratory gated acquisition. In addition, our results demonstrate that the application of the spatial transformation in the raw data domain within the reconstruction leads to superior contrast in comparison to simply adding together already reconstructed and realigned images of the individual gated frames.

5. Conclusion

A list-mode-data-based respiratory motion correction using elastic transformations during image reconstruction has been implemented and its performance evaluated. The developed algorithm includes the implementation of modified normalization and attenuation corrections taking into consideration the applied transformations. Our results with a digital phantom,

including realistic non-rigid respiratory motion, demonstrate that the use of an interpolation step in the calculation of the sensitivity matrix coefficients leads to artefacts and a reduced quantitative improvement in the motion corrected reconstructed images.

A comparison of the reconstructed images with and without correction revealed significant respiratory motion compensation in the lung lesions. In comparison to the use of an affine model, the elastic-transformation-based solution leads to a more uniform improvement across the lung fields for the different lesion sizes considered. In addition, the application of the displacements in the image space followed by summing the realigned gated frames leads to $<30\%$ contrast loss relative to the incorporation of the displacements in the reconstruction process.

References

Asma E, Manjeshwar R and Thielemans K 2006 Theoretical comparison of motion correction techniques for PET image reconstruction *IEEE Med. Image Conf. Rec.* **3** 1762–7

Boucher L, Rodrigue S, Lecomte R and Benard F 2004 Respiratory gating for 3-dimensional PET of the thorax: feasibility and initial results *J. Nucl. Med.* **45** 214–9

Bruyant P, King M and Pretorius P 2003 Correction of the respiratory motion of the heart by tracking of the center of mass of thresholded projections: a simulation study using the dynamic MCAT phantom *IEEE Trans. Nucl. Sci.* **49** 2159–66

Bruyant P, Turzo A, Bizais Y, Cheze Le Rest C and Visvikis D 2006 A comparison of three respiratory gating methods in PET imaging for oncology *J. Nucl. Med.* **47** 183P

Dawood M, Lang N, Jiang X and Schafers K P 2006 Lung motion correction on respiratory gated 3-D PET/CT images *IEEE Trans. Med. Imaging* **25** 476–85

Erdi Y E *et al* 2004 The CT motion quantitation of lung lesions and its impact on PET-measured SUVs *J. Nucl. Med.* **45** 1287–92

Goerres G W, Kamel E, Heidelberg T N, Schwitter M R, Burger C and von Schulthess G K 2002 PET-CT image co-registration in the thorax: influence of respiration *Eur. J. Nucl. Med. Mol. Imaging* **29** 351–60

Han G, Liang Z and You J 1999 A fast raytracing technique for TCT and ECT studies *IEEE Nucl. Sci. Symp. Conf. Rec.* **3** 1515–8

Jacobson M and Fessler J 2003 Joint estimation of image and deformation parameters in motion-corrected PET *IEEE Nucl. Sci. Symp. Conf. Rec.* **5** 3290–4

Klein G and Huesman R 1997 A 3D optical flow approach to addition of deformable PET volumes *Proc. IEEE Nonrigid and Articulated Motion Workshop (Puerto Rico)* pp 136–43

Kybic J and Unser M 2003 Fast parametric elastic image registration *IEEE Trans. Image Process* **12** 1427–42

Lamare F, Cresson T, Savean J, Cheze Le Rest C, Reader A J and Visvikis D 2007 Respiratory motion correction for PET oncology applications using affine transformation of list mode data *Phys. Med. Biol.* **52** 121–40

Lamare F, Ledesma Carbayo M, Kontaxakis G, Santos A, Turzo A, Bizais Y, Cheze Le Rest C and Visvikis D 2005 Incorporation of elastic transformations in list-mode based reconstruction for respiratory motion correction in PET *IEEE Nucl. Sci. Symp. Conf. Rec.* **3** 1740–4

Lamare F, Turzo A, Bizais Y, Le Rest C C and Visvikis D 2006 Validation of a Monte Carlo simulation of the Philips Allegro/GEMINI PET systems using GATE *Phys. Med. Biol.* **51** 943–62

Ledesma-Carbayo M J, Mahia-Casado P, Santos A, Perez-David E, Garcia-Fernandez M A and Desco M 2006 Cardiac motion analysis from ultrasound sequences using nonrigid registration: validation against Doppler tissue velocity *Ultrasound Med. Biol.* **32** 483–90

Li T, Thorndyke B, Schreibmann E, Yang Y and Xing L 2006 Model-based image reconstruction for four-dimensional PET *Med. Phys.* **33** 1288–98

Livieratos L, Stegger L, Bloomfield P M, Schafers K, Bailey D L and Camici P G 2005 Rigid-body transformation of list-mode projection data for respiratory motion correction in cardiac PET *Phys. Med. Biol.* **50** 3313–22

McClelland J R, Blackall J M, Tarte S, Chandler A C, Hughes S, Ahmad S, Landau D B and Hawkes D J 2006 A continuous 4D motion model from multiple respiratory cycles for use in lung radiotherapy *Med. Phys.* **33** 3348–58

Nehmeh S A *et al* 2002 Effect of respiratory gating on reducing lung motion artefacts in PET imaging of lung cancer *Med. Phys.* **29** 366–71

Nehmeh S A *et al* 2004 Four-dimensional (4D) PET/CT imaging of the thorax *Med. Phys.* **31** 3179–86

Pan T, Mawlawi O, Nehmeh S A, Erdi Y E, Luo D, Liu H H, Castillo R, Mohan R, Liao Z and Macapinlac H A 2005 Attenuation correction of PET images with respiration-averaged CT images in PET/CT *J. Nucl. Med.* **46** 1481–7

Qi J and Huesman R 2002 List Mode reconstruction for PET with motion compensation: a simulation study *Proc. IEEE Int. Symp. Biomed. Imaging* pp 413–6

Qiao F, Pan T, Clark Jr W J and Mawlawi O R 2006 A motion-incorporated reconstruction method for gated PET studies *Phys. Med. Biol.* **51** 3769–83

Rahmim A, Bloomfield P, Houle S, Lenox M, Michel C, Buckley K, Ruth T and Sossi V 2004 Motion compensation in histogram-mode and list-mode reconstructions: beyond the event-driven approach *IEEE Trans. Nucl. Sci.* **51** 2588–96

Reader A, Ally S, Bakatselos F, Manavaki R, Walledge R, Jeavons A, Julyan P, Zhao S, Hastings D and Zweit J 2002 One-pass list-mode EM algorithm for high-resolution 3D PET image reconstruction into large array *IEEE Trans. Nucl. Sci.* **49** 693–9

Schoder H, Erdi Y E, Chao K, Gonen M, Larson S M and Yeung H W 2004 Clinical implications of different image reconstruction parameters for interpretation of whole-body PET studies in cancer patients *J. Nucl. Med.* **45** 559–66

Segars W, Lalush D and Tsui B 2001 Modelling respiratory mechanics in the MCAT and spline-based MCAT phantoms *IEEE Trans. Nucl. Sci.* **48** 89–97

Siddon R 1986 Fast calculation of the exact radiological path for a three-dimensional CT array *Med. Phys.* **12** 252–5

Sorzano C, Thevenaz P and Unser M 2005 Elastic registration of biological images using vector-spline regularization *IEEE Trans. Biomed. Eng.* **52** 652–63

Studholme C, Hill D and Hawkes D 1999 An overlap invariant entropy measure of 3D medical image alignment *Pattern Recognit.* **32** 71–86

Unser M, Aldroubi A and Eden M 1993 The L_2 polynomial spline pyramid *IEEE Trans. Pattern Anal. Mach. Intell.* **15** 364–79

Visvikis D, Barret O, Fryer T, Lamare F, Turzo A, Bizais Y and Cheze-LeRest C 2004 Evaluation of respiratory motion effects in comparison with other parameters affecting PET image quality *IEEE Nucl. Sci. Symp. Conf. Rec.* **6** 3668–72

Visvikis D, Cheze-LeRest C, Costa D C, Bomanji J, Gacinovic S and Ell P J 2001 Influence of OSEM and segmented attenuation correction in the calculation of standardised uptake values for [18F]FDG PET *Eur. J. Nucl. Med.* **28** 1326–35

Visvikis D, Lamare F, Turzo A, Barrett O, Fryer T, Bizais Y and Cheze Le Rest C 2005 Efficiency of respiratory gating for motion correction in PET *J. Nucl. Med.* **46** 163P

Visvikis D, Ledesma Carbayo M, Lamare F, Mawlawi O, Jarritt P, Bruyant P, Santos A, Kontaxakis G, Boussion N and Cheze-LeRest C 2006 A spatiotemporal image registration algorithm for correction of respiratory motion in PET/CT *J. Nucl. Med.* **47** 234P

Zhao H and Reader A 2002 Fast Projection algorithm for voxel arrays with object dependent boundaries *IEEE Nucl. Sci. Symp. Conf. Rec.* **2** 1490–4